Sci. Rep. Kanazawa Univ.
Vol. 69, pp. 13–23, 2026

ARTICLES

Simulations of Tornado-type Flows in Non-axisymmetric Domains

Afifah Maya IKNANINGRUM*, Pen-Yuan HSU, Tsuyoshi YONEDA, and Hirofumi NOTSU

Graduate School of Natural Science and Technology, Kanazawa University, Kanazawa, Japan
Graduate School of Mathematical Science, The University of Tokyo, Tokyo, Japan
Graduate School of Economics, Hitotsubashi University, Tokyo, Japan
Faculty of Mathematics and Physics, Kanazawa University, Kanazawa, Japan

(Received December 30, 2025 and accepted in revised form February 27, 2026)

Abstract While tornado-type flow has been extensively studied in axisymmetric domains, the influence of curvature on vortex dynamics remains less understood. This study numerically solves the incompressible Navier–Stokes equations with no-slip boundaries using the Finite Element Method and swirling initial velocity to explore this effect. Simulations in non-axisymmetric (curved cylindrical) domains reveal two phenomena: gradual outward displacement of the main vortex from the geometric axis (center of the domain) and energy transfer dynamics between radial regions. Greater curvature makes these effects more pronounced.

Keywords. Tornado-type flow, Navier–Stokes, Finite Element Method, Vortex Dynamics, Energy Transfer

1 Introduction

Research into tornadoes has employed observational (field-based), experimental (laboratory-based), and computational (numerical simulation) approaches. In observational studies, the pioneering work of Fujita et al. [4] laid the foundation for quantifying tornado intensity, which was later expanded through radar observations and storm chaser reports [1, 2]. These studies have revealed essential features of tornado structure and evolution.

In parallel, laboratory-based experiments have been conducted to recreate tornado-like flows under controlled conditions [3, 12, 13]. In computational studies, many simulations are conducted in axisymmetric domains [5, 11] and typically evaluate the sensitivity to flow parameters such as swirl ratio [7, 14]. In this research, we aim to investigate the behavior of tornado-type flow in non-axisymmetric domains involving curvature.

Prior research by Hsu, Notsu and Yoneda [5] on axisymmetric tornado-type flow in a straight cylindrical domain has yielded valuable insights in idealized settings. Using hyperbolic inflow

*Corresponding author Email: afifahmaya35@gmail.com

with and without swirl, they studied flow behavior near a saddle point. It is observed that only in the swirl case did the distance from the z-axis to the location of maximum velocity change drastically at a specific time (called the turning point). Building on their approach using the Finite Element Method (FEM), we incorporate curvature into our simulations, considering that real tornadoes are often non-axisymmetric. While curvature significantly influences flow structures, energy distribution, and vortex behavior, its effects are not yet fully understood. By addressing this gap, our research enhances the understanding of vortex behavior in non-axisymmetric domains involving curvature.

Using FEM, we simulate the incompressible Navier–Stokes equations with no-slip boundary conditions and swirling initial velocity on curved cylindrical domains to investigate tornado-like flows. Tornadoes form when a latent vortex in the lower atmosphere is stretched vertically by updrafts into a compact and powerful vortex. To replicate this mechanism, our model incorporates initial velocities with both upward and rotating flow components (hyperbolic flow with swirl). The swirl is imposed only at the initial time, with no external forcing, inflow, or outflow applied thereafter, allowing the vortex to evolve naturally. While not being a direct atmospheric simulation, this approach serves as a fundamental study of how curvature affects the dynamics of a contained, decaying vortex that shares characteristics with tornado-like flows.

Based on simulation results, we aim to understand the effect of curvature. Observing the velocity field, we find that domain curvature exerts a greater influence than the initial velocity profile. It is shown that the location where the maximum magnitude of velocity occurs (hereafter, it will be abbreviated as the maximum velocity location) for the curved domains gradually shifts outward, and higher curvature accelerates this motion. Related to this, we also define the central curve using low-pressure points. It is shown that both the maximum velocity location and the central curve exhibit outward directional movement.

To analyze the tornado-type flow, we visualize the vortex dynamics by utilizing the Q-criterion method. Based on Q-criterion observations, we divide the domains into regions where the location of the main vortex and smaller vortices are estimated. These regions are divided based on distance from the central curve to observe the energy distribution. Finally, by calculating the energy across these regions, we capture the phenomenon of energy transfer: kinetic energy is transferred from the inner region, where the main vortex is located, to the outer region, where smaller vortices are developed.

2 Numerical Simulations

2.1 Governing equations and numerical method

We consider the incompressibe Navier–Stokes equations with no-slip boundary condition:

$$\begin{cases} \partial_t \boldsymbol{v} + (\boldsymbol{v}\cdot\boldsymbol{\nabla})\boldsymbol{v} - \nu\Delta\boldsymbol{v} + \boldsymbol{\nabla} p = 0,\ \boldsymbol{\nabla}\cdot\boldsymbol{v} = 0 \ \text{ in } \Omega\times(0,T), \\ \boldsymbol{v} = \boldsymbol{0} \ \text{ on } \partial\Omega\times(0,T),\ \boldsymbol{v} = \boldsymbol{v}^0 \ \text{ in } \Omega \text{ at } t = 0. \end{cases} \tag{2.1}$$

Here, $\boldsymbol{v} = \boldsymbol{v}(\boldsymbol{x},t) : \Omega\times(0,T) \to \mathbb{R}^3$ and $p = p(\boldsymbol{x},t) : \Omega\times(0,T) \to \mathbb{R}$ represent the velocity and pressure, respectively. $\nu > 0$ is the viscosity, $\boldsymbol{v}^0 : \Omega \to \mathbb{R}^3$ is the prescribed initial velocity, and Ω denotes cylindrical domains, which will be defined in Section 2.2. The boundary condition $\boldsymbol{v} = \boldsymbol{0}$ on $\partial\Omega\times(0,T)$ implies a closed container, with no inflow or outflow.

The FEM used in this simulation is the following prior research [5] which is the stabilized Lagrange–Galerkin scheme [8, 9, 10], to find a pair of piecewise linear functions $(\boldsymbol{v}_h^k, p_h^k)$, approx-

imation of $(\boldsymbol{v}, p)$ at $t = k\tau$, in a *strong*-representation:

$$\frac{1}{\tau}\left[\boldsymbol{v}_h^k(\boldsymbol{x}) - \boldsymbol{v}_h^{k-1}\left(\boldsymbol{x} - \boldsymbol{v}_h^{k-1}(\boldsymbol{x})\tau\right)\right] - \nu\Delta\boldsymbol{v}_h^k + \boldsymbol{\nabla} p_h^k = 0,$$
$$\boldsymbol{\nabla}\cdot\boldsymbol{v}_h^k - \delta_0^{\mathrm{s}} h^2 \Delta p_h^k = 0,$$

for $k = 1, 2, \ldots, N_T$, where $\tau, h, \delta_0^{\mathrm{s}} > 0$, and $N_T := \lfloor T/\tau \rfloor \in \mathbb{N}$ are time-step size, mesh size, stabilization parameter, and total number of time steps, respectively. It is worth noting that the scheme converges to the exact solution with accuracy of order $O(\tau + h)$ in $L^\infty(0,T;H^1(\Omega;\mathbb{R}^3))$ and of order $O(\tau + h^2)$ in $L^\infty(0,T;L^2(\Omega;\mathbb{R}^3))$ under some conditions, see [10]. In this paper, we chose $\tau = 1.25 \times 10^{-2}$ and $\delta_0^{\mathrm{s}} = 1$.

2.2 Domain configurations

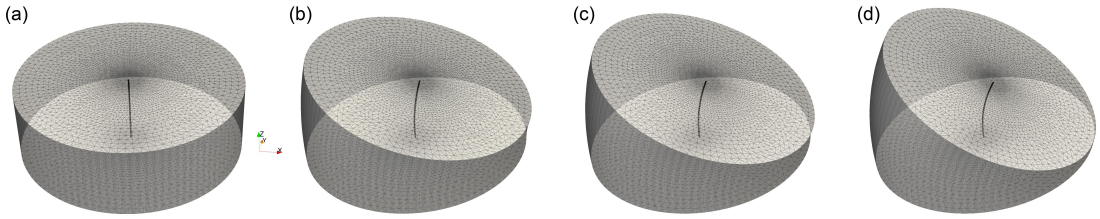

Figure 1: 3D visualization of the domain shapes of (a) the straight cylindrical domain Ω_S and the curved cylindrical domain Ω_C with its geometric axis (black curve in center): (b) Ω_C with $R = 2.0$, (c) Ω_C with $R = 1.5$, and (d) Ω_C with $R = 1.1$.

The domains considered in this study are the straight cylindrical domain and the curved cylindrical domains. The straight cylindrical domain Ω_S (Figure 1a) is defined as

$$\Omega_S := \{\boldsymbol{x}_S = (x, y, z) \in \mathbb{R}^3 \mid -a \le z \le 4a,\ r(\boldsymbol{x}_S) \le r_{\max}\} \tag{2.2}$$

where radius $r(\boldsymbol{x}_S) = \sqrt{x^2 + y^2}$, maximum radius $r_{\max} \in \mathbb{R}$ and $a > 0$. To model the curved cylindrical domains Ω_C (Figures 1b-d) which are conceptualized as a toroidal segment, we apply the mapping $T_{S,R} : \Omega_S \to \Omega_C$, given by

$$T_{S,R}(\boldsymbol{x}_S) := \left(R - (R - x)\cos(\frac{z}{R}),\ y,\ (R - x)\sin(\frac{z}{R})\right) \tag{2.3}$$

where $\boldsymbol{x}_S \in \Omega_S$ and $R > r_{\max}$ is torus radius. The curved cylindrical domains are defined as

$$\Omega_C := \{\boldsymbol{x}_C \in \mathbb{R}^3 \mid \boldsymbol{x}_C = T_{S,R}(\boldsymbol{x}_S),\ r_{\max} \le R\}. \tag{2.4}$$

For all simulations, we set $r_{\max} = 1$, $a = 0.125$, and Reynolds number $Re = 10^4$. To ensure turbulent flow while maintaining reasonable computational efficiency, only a single representative Reynolds number is used. This approach allows us to concentrate on the influence of curvature variation, which is the primary focus of this study. Note that in the simulations, the number of points N_p is 481265, the number of elements N_e is 2828400, the maximum mesh size is 0.0873, the minimum mesh size is 0.00208, and the average mesh size is 0.0208.

We consider three torus radii $R = 2$, 1.5, and 1.1, where smaller values of R correspond to larger curvature. As our curved cylindrical domains are conceptualized as a toroidal segment,

by the definition of toroidal curvature $\delta = r_{\max}/R$, our simulations consider curvatures of $\delta =$ 0.5, 0.667, and 0.909. In this study, we distinguish between the geometric axis (Figure 1), which refers to the fixed and time-independent axis at the center of each domain, and the central curve (Figure 6), which is flow-dependent and may evolve over time.

2.3 Initial configuration

For simulations, we consider swirl initial velocity

$$\boldsymbol{v}^0 := u_r \boldsymbol{e}_r + u_\theta \boldsymbol{e}_\theta + u_z \boldsymbol{e}_z, \tag{2.5}$$

where $\boldsymbol{e}_r = (1/\sqrt{x^2+y^2})(x,y,0)$, $\boldsymbol{e}_\theta = (1/\sqrt{x^2+y^2})(-y,x,0)$, $\boldsymbol{e}_z = (0,0,1)$ with:

$$\begin{aligned} u_z &= \psi(r,\varepsilon_1,-\beta_1)\psi(z,\varepsilon_2,-\beta_2), \\ \rho &= \psi(r,\varepsilon_3,-\beta_3)\psi(z,\varepsilon_4,\beta_4), \\ u_\theta &= \psi(r,\varepsilon_5,-\beta_5)\psi(z,\varepsilon_6,-\beta_6), \\ u_r &= \mathrm{sign}(z)\rho u_z, \end{aligned}$$

for $\psi(a,\varepsilon,\sigma) = (a^2+\varepsilon)^\sigma$.

The constants ε_i and β_i $(i = 1,\ldots,6)$ are set to 1. By this setting, the initial magnitude of velocity $|\boldsymbol{v}|$ at $(x,y,z) = (0,0,0)$ (called the center of the initial velocity) is larger than at other places (see Figure 2). This configuration is chosen so that the center of the initial velocity is located close to the lower boundary but not on the boundary. Note that the initial velocity and straight cylindrical domain configurations are like those used in prior research [5] where it numerically satisfies the divergence-free and no-slip boundary condition after the first time step, not at the initial step. The initial configuration in (2.5) is defined for the straight initial velocity profile, and we use the mapping $T_{S,R}$ (Eq. (2.3)) to define the curved initial velocity profiles.

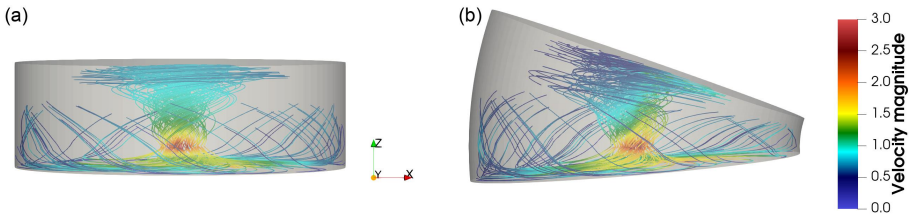

Figure 2: 3D swirl initial velocity streamlines in (a) the straight cylindrical domain Ω_S and (b) the curved cylindrical domain Ω_C with $R = 1.5$.

3 Results and Discussion

The simulation results are presented to understand the effect of curvature of the domain by observing the velocity, pressure, kinetic energy, angular momentum, and vortex dynamics.

3.1 Velocity observations

For the curved cylindrical domain Ω_C with $R = 1.5$, the initial velocity streamlines are shown in Figure 2b and the evolution of velocity magnitude in the xz-plane is shown in Figure 3. By

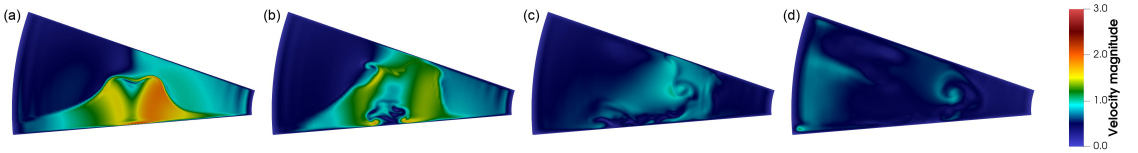

Figure 3: Time evolution of the xz-plane slice of velocity magnitude $|\boldsymbol{v}|$ for the curved cylindrical domains Ω_C ($R = 1.5$) at (a) $t = 0.3$, (b) $t = 0.8$, (c) $t = 1.9$, and (d) $t = 2.9$.

default, the swirl initial velocity profile for the simulation is designed to align the domain shape (Figure 2). However, to investigate the influence of the initial velocity profile on the simulations, we compare results by pairing domain shapes (Ω_S and Ω_C) with initial velocity profiles (straight and curved). We analyze the maximum magnitude of velocity, denoted by $|\boldsymbol{v}|_\infty(t) = |\boldsymbol{v}|_\infty$, and its distance from the geometric axis or the maximum velocity location, $d(|\boldsymbol{v}|_\infty)$. The results in Figure 4 show that the simulation outcomes–specifically the maximum velocity magnitude $|\boldsymbol{v}|_\infty$ and its location $d(|\boldsymbol{v}|_\infty)$–are similar for the same domain shape, regardless of the initial velocity profile. This suggests that the domain geometry has a greater influence on the simulation results than the choice of initial velocity profile.

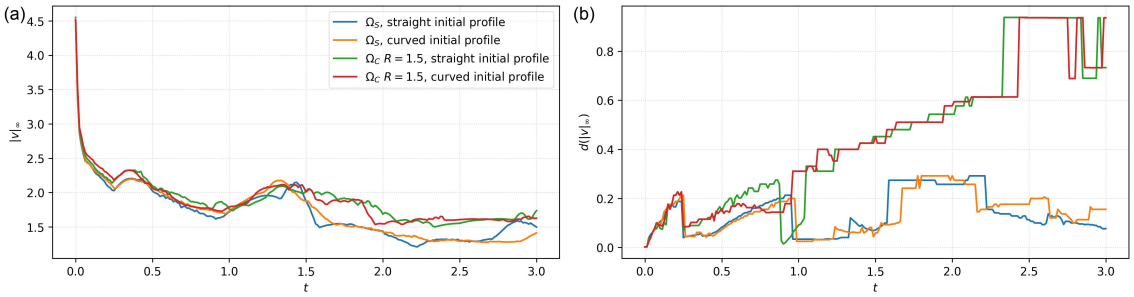

Figure 4: Time evolution of (a) the maximum magnitude of velocity $|\boldsymbol{v}|_\infty$ and (b) its distance to the geometric axis $d(|\boldsymbol{v}|_\infty)$, for combinations of domain (straight cylindrical domain Ω_S and curved cylindrical domain Ω_C with $R = 1.5$) and initial velocity profile (straight and curved).

The influence of domain shape is investigated through simulations of the curved cylindrical domains Ω_C with varying curvature. Results in Figure 5 show that in Ω_C, the maximum velocity location moves progressively farther from the geometric axis, unlike in Ω_S, where it remains close. This suggests that curvature of the domains causes the maximum velocity location to move outward. Furthermore, higher curvature (smaller R) results in larger $d(|\boldsymbol{v}|_\infty)$, indicating that the maximum velocity location shifts farther from the geometric axis.

3.2 Pressure observations

To further understand the flow behavior, we analyze a line of low-pressure, which we define as the central curve. The central curve is calculated at each time step t, so the time notation will be omitted. First, let us consider a set of nodes $M := \{\boldsymbol{P} \in \mathbb{R}^3 \mid \boldsymbol{P} \text{ is a node point}\}$.

Using the definitions in (2.2), (2.3), and (2.4), the cross section plane-l in the straight cylindrical domain is defined as $\Pi_l^S = \{(x,y,z) \in \Omega_S \mid z = z_l,\ x^2 + y^2 \leq r_{\max}\}$. Then, the definition for the curved cylindrical domain $\Pi_l^C = T_{S,R}(\Pi_l^S)$ for $l = 0,\ldots,N_l$ (where $N_l = 100$). Note that vertical height $z_l \in [-a, 4a]$ is equally divided by N_l. The minimum pressure point in each plane-l is given

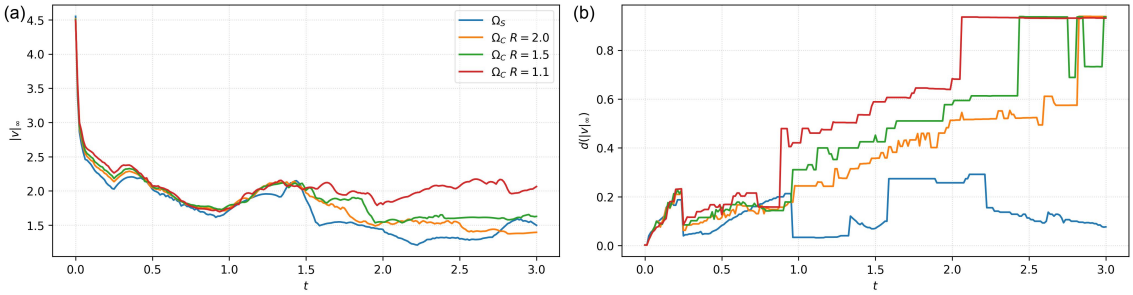

Figure 5: Time evolution of (a) the maximum magnitude of velocity $|\boldsymbol{v}|_\infty$ and (b) its distance to the geometric axis $d(|\boldsymbol{v}|_\infty)$, for the straight cylindrical domain Ω_S and the curved cylindrical domains Ω_C with $R = 2$, $R = 1.5$, and $R = 1.1$.

by:

$$\boldsymbol{P}_{\min,l} := \underset{\boldsymbol{P}\in M_l}{\operatorname{argmin}}\{p(\boldsymbol{P})\},$$

where $M_l := M \cap \Pi_l$ represents the intersection of node points and the cross section plane. Here, $\Pi_l = \Pi_l^S$ is for the straight cylindrical domain and Π_l^C is for the curved cylindrical domains. Note that pressure at the point $\boldsymbol{P}_{\min,l}$ is smaller compared to pressure at any point in plane, i.e. $p(\boldsymbol{P}_{\min,l}) \leq p(\boldsymbol{P})$ for all $\boldsymbol{P} \in M_l$.

To define a continuous central curve from the discrete pressure minimum points, which exhibit numerical noise from the discrete mesh, we applied a least-squares fit using a cubic polynomial. This fitting approach was chosen to generate a smooth trajectory from the rough raw data. The representation of the central curve, $\{\boldsymbol{C}(\xi_l) \in \mathbb{R}^3 \mid \xi_l := z_l\}$, is given by:

$$\boldsymbol{C}(\xi_l) = \begin{bmatrix} c_0^{(1)} + c_1^{(1)}\xi_l + c_2^{(1)}\xi_l^2 + c_3^{(1)}\xi_l^3 \\ c_0^{(2)} + c_1^{(2)}\xi_l + c_2^{(2)}\xi_l^2 + c_3^{(2)}\xi_l^3 \\ c_0^{(3)} + c_1^{(3)}\xi_l + c_2^{(3)}\xi_l^2 + c_3^{(3)}\xi_l^3 \end{bmatrix}.$$

The coefficients $\boldsymbol{c} = [c_0^{(1)}, \ldots, c_3^{(3)}]$ were determined by minimizing $J(\boldsymbol{c}) := \frac{1}{2}(\sum_l |\boldsymbol{C}(\xi_l) - \boldsymbol{P}_{\min,l}|^2)$.

Detailed projections of the central curve for the curved cylindrical domain Ω_C with $R = 1.5$ are shown in Figure 6, revealing a shift toward the negative x-axis and positive y-axis. The average movement speeds in the same directions for $R = 2$, 1.5, and 1.1 are 0.366, 0.418, and 0.49, respectively, indicating that smaller R results in faster outward motion. This trend aligns with the earlier observation of $d(|\boldsymbol{v}|_\infty)$ (Figure 5b) and further supports the connection between low-pressure regions and high-velocity regions. At present, faster outward motion has been observed as a fact, and we anticipate this may be a type of centrifugal instability. However, rigorous physical insights—such as whether centrifugal force can be expressed using only part of the cylinder—remain a future challenge.

3.3 Vortex identification using Q-criterion

For further study of dynamics in the curved cylindrical domains, we employ the Q-criterion method [6] to objectively identify vortices. Q-criterion was selected for vortex identification based on its theoretical advantages over vorticity magnitude in wall-bounded flows as mentioned by Jeong and Hussain [6]. Unlike vorticity magnitude, which exhibits maximum values at walls regardless of actual vortical motion, Q-criterion vanishes at stationary walls where shear strain and

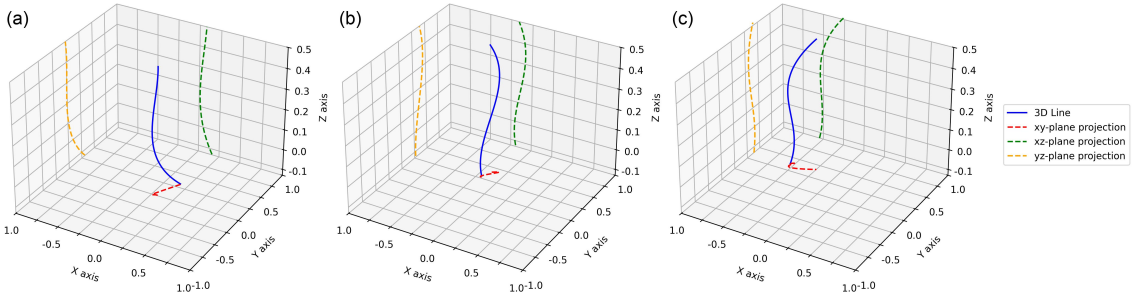

Figure 6: Time evolution of the 3D central curve (blue) with its projection on 2D planes for the curved cylindrical domain Ω_C with $R = 1.5$ at (a) $t = 0$, (b) $t = 1.9$, and (c) $t = 3$.

vorticity have equal magnitude. This distinction is critical for these simulations, where the presence of walls could cause vorticity magnitude to misidentify shear-dominated regions as vortex cores.

The Q-criterion method evaluates the local balance between rotational and straining motions through the velocity gradient tensor. It is defined as:

$$Q = \frac{1}{2}\left(|\mathbf{W}|^2 - |\mathbf{S}|^2\right) = \frac{1}{2}\left(\sum_{ij}\mathbf{W}_{ij}^2 - \sum_{ij}\mathbf{S}_{ij}^2\right) \tag{3.1}$$

where $\mathbf{W} = \frac{1}{2}\left(\nabla \boldsymbol{v} - (\nabla \boldsymbol{v})^T\right)$ is the antisymmetric part (representing rotational motion) and $\mathbf{S} = \frac{1}{2}\left(\nabla \boldsymbol{v} + (\nabla \boldsymbol{v})^T\right)$ is the symmetric part (representing strain rate). A vortex is identified when rotational motion dominates over strain, indicated by $Q > 0$. Higher value of Q indicates a vortex with stronger rotational force.

Visualizing the Q-criterion for $Q \geq 50$ in the curved cylindrical domain Ω_C with $R = 1.5$, we obtain Figure 7, shown for $t = 0.8$ and $t = 1.9$. In the visualization, we can observe the vortex dynamics and the fact that the central curve (black line) is in the center of region with most vortices. This region is estimated to be the location of the main vortex (most coherent structure imposed by initial velocity), located within 0.15 of the central curve. Then, the vortices will spread out further to distances around 0.4 and further around 0.7. These distance estimates will later be used to divide the domains to observe the energy dynamics in the simulations.

The Q-criterion analysis clearly distinguishes vortex structures based on intensity, with strong vortices (blue, $Q \geq 750$) and weaker vortices (red, $Q \geq 250$) visible in Figure 8. At $t = 0.3$, the main vortex aligns with the central curve at the pressure minimum. By $t = 0.9$, it is observed that the main vortex and the central curve are moving outward from the geometric axis while smaller vortices (smaller structures compared to the main vortex with shorter lifespan, which are not present in the initial condition) appear around the main vortex. This displacement correlates with both the velocity trends (Figure 5b) and the central curve movement derived from low-pressure regions (Figure 6).

3.4 Energy transfer observation

To roughly investigate flow dynamics, we divide the domains into three regions. Observing the location of the main vortex and smaller vortices (Figure 8), we define three regions based on the radial distance $|r_e|$ from the central curve: the inner region $r_{e,1}$ for $|r_e| \leq 0.15$, the middle region $r_{e,2}$ for $0.15 < |r_e| \leq 0.4$, and the outer region $r_{e,3}$ for $0.4 < |r_e| \leq 0.7$. With this division, the main vortex is located primarily in the inner region, and smaller vortices are found mostly in the middle region. This enables clearer analysis of energy distribution and transfer between regions. Notably,

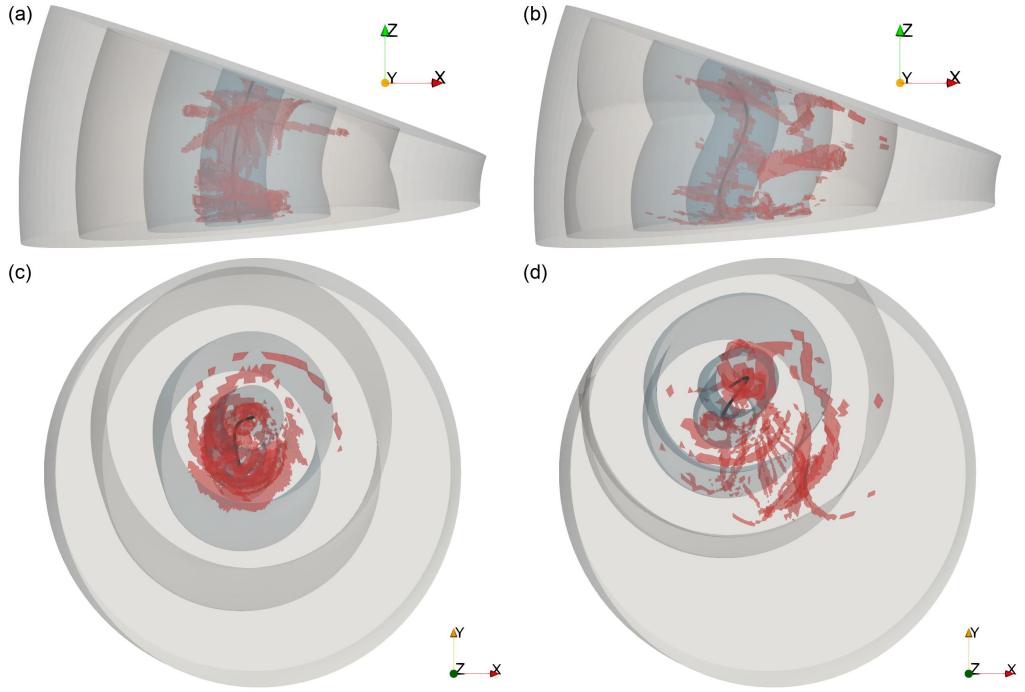

Figure 7: 3D vortices in the curved cylindrical domain Ω_C ($R = 1.5$) using Q-criterion for $Q \geq 50$ (red) at $t = 0.8$ (a, c) and $t = 1.9$ (b, d) with front-(a, b) and top-views(c, d). The central curve (black), the inner $r_{e,1}$ (blue), the middle $r_{e,2}$ (light blue), and the outer $r_{e,3}$ (gray) regions are shown.

the inner region has the smallest volume (4.59%), the middle region is larger (28.06%), and the outer region has the largest volume (67.35%).

By calculating the kinetic energy in each region, we can observe the energy transfer between them. The kinetic energy E quantifies the total fluid motion, where higher values indicate more energetic flow structures:

$$E = \int_{\Omega_C} \frac{1}{2}|\boldsymbol{v}|^2 \, d\Omega_C \approx \frac{1}{2}\sum^{N_e} |\boldsymbol{v}_e|^2 \, V_e \tag{3.2}$$

with total number of elements N_e where $\boldsymbol{v}_e$ is the velocity vector and V_e the volume of the tetrahedral element. Figure 9 shows the gradual decay of energy in all simulations.

Figure 10 shows the total kinetic energy in each region and Figure 11 shows energy density, which is normalized energy over the volume. Observing both graphs, the transfer of energy across regions can be captured. At early times, as the energy in the inner region (blue line) decreases, the energy in the middle region (orange line) increases. This shows the energy transfer from the inner region ($r_{e,1}$) to the middle region ($r_{e,2}$). After that, the transfer from the middle region ($r_{e,2}$) to the outer region ($r_{e,3}$) occurs, indicated by the orange line decreasing while the green line increases.

Regarding the timing of the energy transfer, the simulations show that in the domain with higher curvature ($R = 1.1$), the transfer happens earlier compared to other domains. These observations show that energy from the inner region, where the main vortex is located, is transferred to the middle and then the outer region, where smaller vortices are developed. The influence of domain curvature manifests in these dynamics. Higher curvature accelerates both the central curve movement and the energy transfer from the inner to the outer regions. Conversely, lower curvature promotes less shift dynamics in a radial sense.

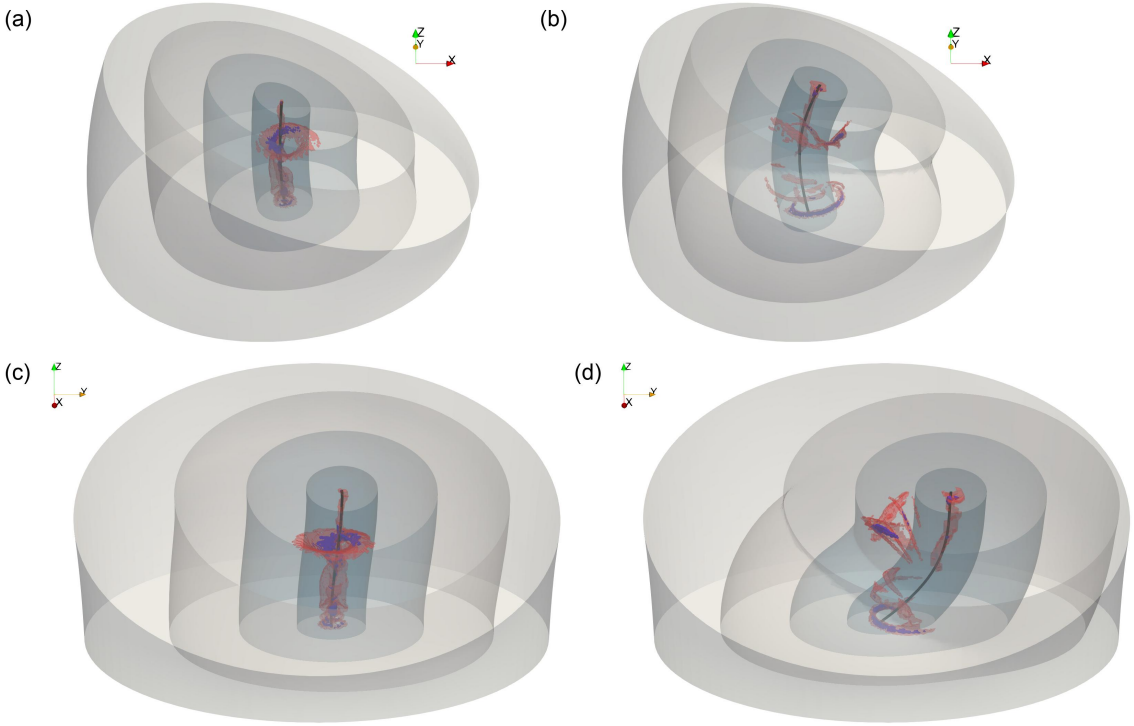

Figure 8: 3D vortices in the curved cylindrical domain Ω_C ($R = 1.5$) using Q-criterion for $Q \geq 250$ (red) and $Q \geq 750$ (dark blue) at $t = 0.3$ (a, c) and $t = 0.9$ (b, d) with front-(a, b) and side-views(c, d). The central curve (black), the inner $r_{e,1}$ (blue), the middle $r_{e,2}$ (light blue), and the outer $r_{e,3}$ (gray) regions are shown.

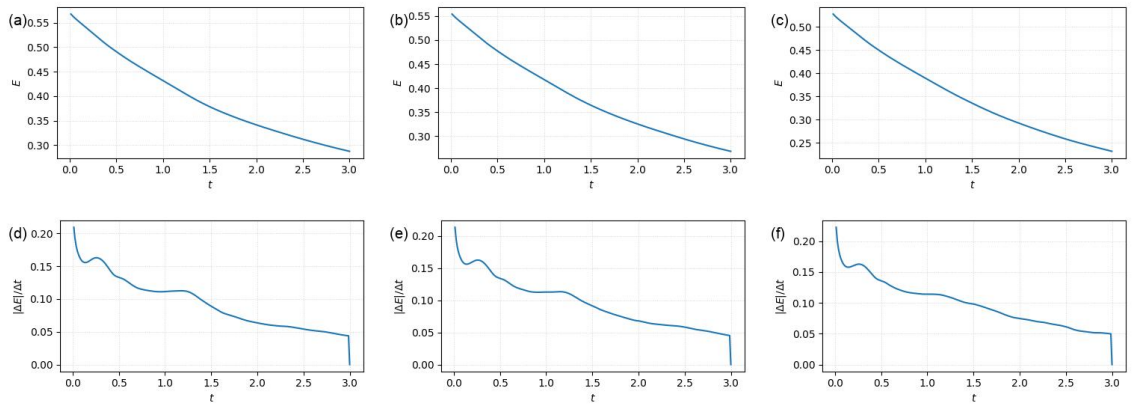

Figure 9: Time evolution of total kinetic energy E and its absolute rate of change $|\Delta E|/\Delta t$, for the curved cylindrical domains Ω_C for torus radii $R = 2$ (a, d), $R = 1.5$ (b, e), and $R = 1.1$ (c, f).

4 Conclusion

Simulations in the curved cylindrical domains Ω_C reveal dynamic behaviors that are absent in prior research [5] in the straight cylindrical domain Ω_S. Specifically, the location of the maximum magnitude of velocity moves outward from the geometric axis, aligning with the displacement of the central curve derived from low-pressure regions. Higher curvature accelerates this outward motion.

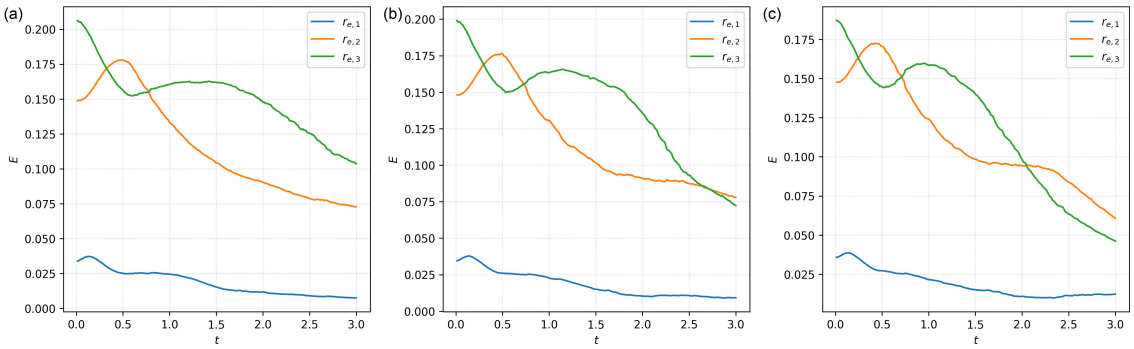

Figure 10: Time evolution of the kinetic energy E for the inner region $r_{e,1}$ (blue), the middle region $r_{e,2}$ (orange), and the outer region $r_{e,3}$ (green) in the curved cylindrical domain Ω_C with (a) $R = 2$, (b) $R = 1.5$, and (c) $R = 1.1$.

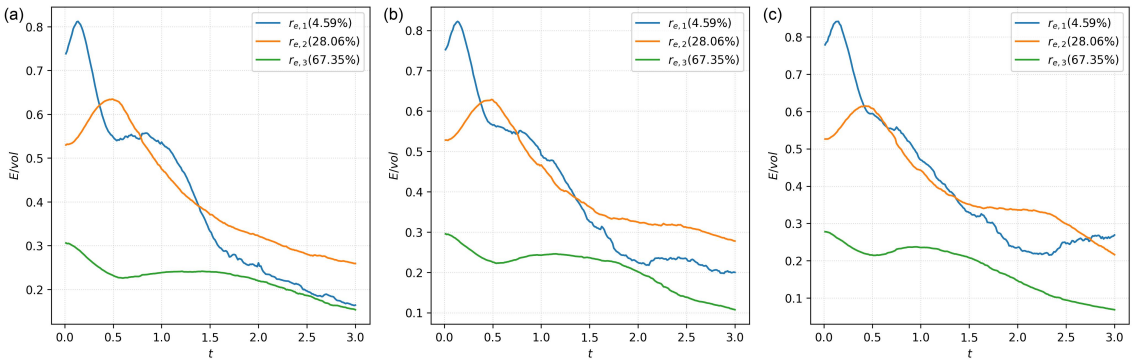

Figure 11: Time evolution of the kinetic energy density $E/volume$ for the inner region $r_{e,1}$ (blue), the middle region $r_{e,2}$ (orange), and the outer region $r_{e,3}$ (green) in the curved cylindrical domain Ω_C with (a) $R = 2$, (b) $R = 1.5$, and (c) $R = 1.1$.

These findings are significant because they demonstrate that non-axisymmetric geometry, a feature of real-world tornadoes, fundamentally alters vortex dynamics. While axisymmetric models provide crucial insights, our results suggest they may miss key mechanisms related to vortex displacement and the redistribution of energy. The curvature-induced energy transfer from the inner region—where the main vortex is located—to the outer region—where smaller vortices develop—could represent a fundamental pathway for vortex decay. As a fundamental study of a decaying vortex in a closed container with no imposed inflow or outflow, this work isolates the effect of curvature. Future research should build upon these findings by incorporating additional physics to better simulate the tornado-type flow.

Appendix

In the simulations, a single representative Re is used. Here the maximum magnitude of velocity $|\boldsymbol{v}|_\infty$ and the maximum velocity location $d(|\boldsymbol{v}|_\infty)$ are shown for different Reynolds numbers $Re =$ 5000, 10000, and 50000 (Figure 12). The results show that a larger Re amplifies the trends, but the overall qualitative behavior of flows remains essentially unchanged. For reasonable computational efficiency, $Re = 10000$ is used in the simulations.

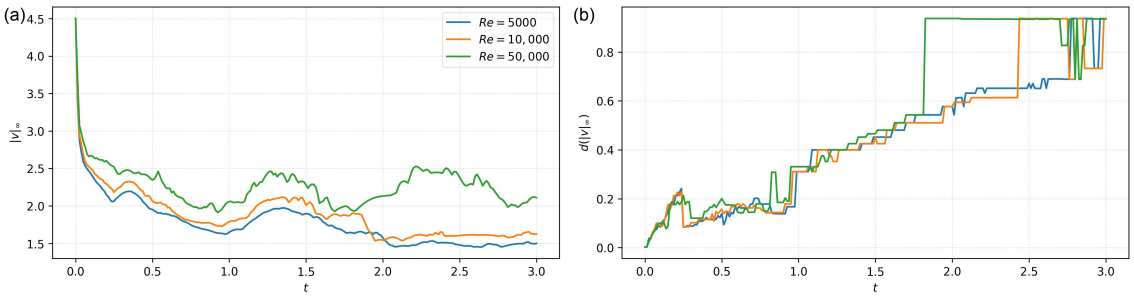

Figure 12: Time evolution of (a) the maximum magnitude of velocity $|\boldsymbol{v}|_\infty$ and (b) its distance to the geometric axis $d(|\boldsymbol{v}|_\infty)$, for the curved cylindrical domain Ω_C with $R = 1.5$ for Reynolds number $Re = 5000$, $Re = 10000$ and $Re = 50000$.

Acknowledgements

Research of TY was partly supported by the JSPS Grants-in-Aid for Scientific Research 24H00186. HN was partly supported by the JSPS Grants-in-Aid for Scientific Research JP20KK0058, JP20H01823, JP21H04431, JP24H00188 and JP25K00920, and JST CREST Grant Number JPMJCR2014.

References

[1] Bluestein, H.B. : Severe Convective Storms and Tornadoes: Observations and Dynamics, Springer, 2013.

[2] Bluestein, H.B., Thiem, K.J., Snyder, J.C. and Houser, J.B. : The Multiple-Vortex Structure of the El Reno, Oklahoma, Tornado on 31 May 2013, Monthly Weather Review 146(8) (2018), 2483–2502.

[3] Church, C.R., Snow, J.T., Baker, G.L. and Agee, E.M. : Characteristic of tornado-like vortices as a function of swirl ratio: A laboratory investigation, Journal of Atmospheric Sciences 36 (1979), 1755–1776.

[4] Fujita, T.T., Bradbury, D.L. and Van Thullenar, C.F. : Palm Sunday tornadoes of April 11, 1965, Monthly Weather Review 98(1) (1970), 29–69.

[5] Hsu, P.-Y., Notsu, H. and Yoneda, T. : A local analysis of the axisymmetric Navier-Stokes flow near a saddle point and no-slip flat boundary, J. Fluid Mech. 729 (2016), 444–459.

[6] Jeong, J. and Hussain, F. : On the identification of a vortex, J. Fluid Mech. 285 (1995), 69–94.

[7] Liu, Z., Cao, S., Liu, H., Hua, X. and Ishihara, T. : Effects of Reynolds number in the range from 1.6×10^3 to 1.6×10^6 on the flow fields in tornado-like vortices by LES: A systematical study, J. Wind Eng. Ind. Aerodyn. 196 (2020), 104028.

[8] Notsu, H. and Tabata, M : A combined finite element scheme with a pressure stabilization and a characteristic-curve method for the Navier–Stokes equations (in Japanese), Trans. Japan. Soc. Ind. Appl. Maths 18 (2008), 427–445.

[9] Notsu, H. and Tabata, M : Error estimates of a pressure-stabilized characteristics finite element scheme for the Oseen equations, J. Sci. Comput. 65 (2015), 940–955.

[10] Notsu, H. and Tabata, M : Error estimates of a stabilized Lagrange–Galerkin scheme for the Navier–Stokes equations, ESAIM: M2AN 50 (2015), 361–380.

[11] Rotunno, R. : Numerical simulation of a laboratory vortex, Journal of Atmospheric Sciences 34 (1977), 1942–1956.

[12] Tari, P.H., Gurka, R. and Hangan, H. : Experimental investigation of tornado-like vortex dynamics with swirl ratio: The mean and turbulent flow fields, J. Wind Eng. Ind. Aerodyn. 98 (2010), 936–944.

[13] Ward, N.B. : The exploration of certain features of tornado dynamics using laboratory model, Journal of Atmospheric Sciences 29 (1972), 1194–1204.

[14] Zhao, Y., Yan, G., Feng, R., Kang, H. and Duan, Z. : Influence of swirl ratio and radial Reynolds number on wind characteristics of multi-vortex tornadoes, Advances in Structural Engineering 26(1) (2023), 89–107.